Turbulent nonpremixed cool flames: Experimental measurements, Direct Numerical Simulation, and manifold-based combustion modeling

Alex G. Novoselov[a,*], Christopher B. Reuter[a], Omar R. Yehia[a], Sang Hee Won[b], Matthew K. Fu[a], Katherine Kokmanian[a], Marcus Hultmark[a], Yiguang Ju[a], Michael E. Mueller[a]

[a] *Department of Mechanical and Aerospace Engineering, Princeton University, Princeton, NJ 08544, USA*
[b] *Department of Mechanical Engineering, University of South Carolina, Columbia, SC 29208, USA*

Abstract

Turbulence, low-temperature chemistry, and their interactions in the form of turbulent cool flames are critical to understanding and improving advanced engines. Design of such engines requires tractable simulations which in turn necessitate turbulent combustion models that can account for cool flames. While manifold-based turbulent combustion models are an attractive option for hot flames, their applicability to cool flames is not yet fully understood. This is partially due to the lack of turbulent cool flame experiments, which has made model validation difficult. This work addresses these points with a combined experimental and computational investigation of turbulent nonpremixed dimethyl ether cool flames. First, a Co-flow Axisymmetric Reactor-Assisted Turbulent (CARAT) burner is developed and tested. Turbulent cool flames are studied using the formaldehyde planar laser-induced fluorescence (PLIF), acetone PLIF, and planar Rayleigh scattering techniques. The acetone PLIF signals are converted into mixture fraction values, and measurements of time-averaged temperature are derived from the Rayleigh scattering signals by taking advantage of the similarities between cool flames and unburned mixtures. Second, a Direct Numerical Simulation (DNS) of the CARAT burner is conducted. The flame is shown to be sensitive to thermal boundary conditions such that the stabilization method is dependent on a 10 K change in inlet temperature. Comparisons of first- and second-order statistics of temperature, mixture fraction, and formaldehyde between the DNS and experiment show good agreement. The validity of manifold-based turbulent combustion models in turbulent cool flames is then explored by first studying the effective Lewis numbers in the flame using a local differential diffusion parameter analysis. Turbulent cool flames are shown to have effective unity Lewis number transport even at a much lower Reynolds number than typically required for hot flames. Good agreement is shown for temperature and formaldehyde between DNS conditional means and one-dimensional nonpremixed flame solutions. Additionally, the motion of the cool flame in mixture fraction space is shown to be well described by one-dimensional nonpremixed flame solutions. These points indicate that the fundamental physics of turbulent cool flames are analogous to turbulent hot flames, implying that the same reduced-order manifold-

*Corresponding author
Email address: agn@princeton.edu (Alex G. Novoselov)

based modeling approaches utilized for turbulent hot flames can be utilized for turbulent cool flames.

Keywords: Turbulent nonpremixed flame, Cool flame, Direct Numerical Simulation (DNS), Reduced-order manifold modeling

1. Introduction

Low-temperature chemistry (LTC) and cool flames are relevant to existing and future engines as they play an important role in ignition in diesel engines [1, 2] and jet engines [3], knock prevention in spark-ignition engines [4, 5], and control of HCCI engines [6]. Laminar cool flames have been studied over a wide range of conditions. Premixed cool flames have been studied experimentally using counterflow configurations, with [7] and without [8] the addition of ozone. These studies were among the earliest stabilized cool flame experiments to elucidate fundamentals about the flame structure and burning limits. Low-pressure systems have allowed for burner-stabilized and freely-propagating flame studies [9], including measurements of isolated laminar cool flame speeds. More recently, transient phenomena have even been studied, including interactions of double cool flame/hot flame structures with unsteady vortices [10]. A major finding was that, under certain thermochemical conditions, a vortex could extinguish only the hot flame, leaving a locally isolated cool flame behind. Computationally, premixed cool flames have been studied in freely-propagating and stretched configurations [11, 8], often supporting the experimental work listed earlier, as well as providing more insight into flame structure and flammability limits.

Laminar nonpremixed cool flames have also been studied extensively experimentally. Counterflow configurations have been used to measure strained ignition and extinction [12], allowing for validation of low-temperature chemical kinetic models [13]. Experiments aboard the International Space Station have looked at spherical flames arising from droplet burning [14], finding a transition between a hot flame and a cool flame over time. More exotic experiments have even shown the possibility of a three-stage nonpremixed flame involving not only hot and cool flames but also a third "warm" flame [15]. Computational studies have often accompanied these experiments [12, 13, 16], adding further understanding about the underlying physics and chemistry of these flames.

While laminar flame studies have provided valuable insight into cool flames, studies of turbulent cool flames are required in order to better understand real combustion devices in which turbulence is present. Studies of this nature are less common than their laminar counterparts. To the authors' knowledge, the first experimental study of isolated turbulent cool flames was a premixed n-heptane flame in a conico-cylindrical reactor [17]. That work was mostly concerned with turbulence measurements in the presence of combustion. However, measurements were difficult in hot flames due to the damage from high temperatures to the measurement instruments, so cool flames were used instead. Since the effect of combustion on turbulence was the focus of the work, the effect of turbulence on the flame was only studied minimally. Later, fuel-

rich stabilized cool flames [18] were used to investigate diesel sprays for fuel reforming applications, but the diagnostics were again limited to temperature measurements with thermocouples. Moreover, neither of these studies explored the structure of turbulent cool flames or gave insight into turbulence-LTC interactions.

A handful of computational studies have investigated turbulence-LTC interactions through simulations. Multi-modal configurations that contain transient turbulent cool flames have become relatively common. Ignition processes in turbulent flows have been shown to transition temporarily to transport-supported cool flames before ultimately undergoing second-stage ignition in two-dimensional nonpremixed mixing layers [19], [20] and three-dimensional temporally evolving jet configurations [21]. However, complex, temporally evolving, multi-modal systems make the study of turbulent cool flame fundamentals difficult.

Recent work has studied isolated premixed turbulent cool flames [22]. A critical takeaway from this work was that a low-temperature chemistry supported ignition front was able to transition to a cool flame with the assistance of turbulent transport and then continue to propagate freely. Isolated nonpremixed turbulent cool flames have also been studied [23] using an instantaneous, local analysis of the flame. This work showed that at a low Damköhler number, just as for hot flames, reduced-order manifold turbulent combustion models are able to fully capture the dynamic behavior of cool flames. However, an open question remains about whether the same is true for higher Damköhler number flames. Additionally, the work was carried out in a two-dimensional domain, did not consider any statistics due to lack of data, and was not compared to experiments, the latter of which is critical to validation of the chemical mechanism used in the simulation under thermochemical conditions accessed in the turbulent flame.

The present work builds on the already existing literature on turbulent nonpremixed cool flames in two ways. First, an isolated turbulent nonpremixed cool flame experimental configuration is presented, which provides a well-characterized experiment to study turbulent cool flame phenomena. Dimethyl ether (DME) is chosen as the fuel due to its combination of strong low-temperature chemistry, gaseous state at room temperature, and the availability of reliable chemical kinetic models to describe its cool flame behavior. The turbulent nonpremixed cool flame structure is examined through formaldehyde (CH_2O) planar laser-induced fluorescence (PLIF), acetone PLIF, and Rayleigh scattering. The acetone PLIF images and Rayleigh scattering images are then converted into two-dimensional measurements of mixture fraction and temperature, respectively. Second, the first truly isolated turbulent nonpremixed cool flame is simulated using Direct Numerical Simulation (DNS) of the CARAT configuration. Both first- and second-order statistics from the DNS and experiment are compared, providing validation for the simulation. Modeling of turbulent nonpremixed cool flames is then explored by examining the validity of effective unity Lewis numbers and through comparison of conditional means from the DNS to one-dimensional nonpremixed flame solutions. Finally, the motion of cool flames in mixture fraction space is examined.

2. Experimental configuration

2.1. CARAT burner

The Co-flow Axisymmetric Reactor-Assisted Turbulent (CARAT) burner is a generational upgrade to the Reactor-Assisted Turbulent Slot (RATS) burner [24, 25] that provides a well-defined co-flow field for computational modeling. The CARAT burner, like the RATS burner, is a Bunsen-type burner with an extended reactor section capable of controlling the pre-flame mixture residence time and temperature. The burner is illustrated in Fig. 1. The inner fuel stream, labeled stream 1, has a diameter $D = 15$ mm. The average velocity of stream 1 ($\bar{U}$) is calculated from the volumetric flow rate of the main flow divided by the exit area. A small annulus (2.0 mm gap width) surrounding the main exit enables the use of a pilot flow, labeled stream 2. The CARAT burner, similar to the Cabra burner [26], also includes a large exterior channel that allows for a heated or vitiated co-flow, labeled stream 3. The co-flow passes through a ceramic honeycomb mesh, which allows for flow laminarization and well-defined boundary conditions.

Two grids are located upstream of the burner exit to generate turbulence within stream 1. The grid located further upstream has a diameter of 34 mm and consists of eight 10° slices for a blockage ratio of approximately 85%. The grid located further downstream has a diameter of 18 mm with eighteen 2 mm diameter holes to give a blockage ratio of 78%. The turbulence in stream 1 is characterized by a nanoscale thermal anemometry probe (NSTAP) [27, 28] operated with a Dantec Dynamics Streamline Pro Constant Temperature Anemometry system. The NSTAP is capable of extremely high spatial and temporal resolution due to the small size of its sensing element (100 nm thick, 2 μm wide, 60 μm long). The NSTAP was positioned at the centerline of the stream 1 exit (approximately even with the exit plane) and sampled at a frequency of 10 kHz, which significantly exceeded all temporal scales in the flow.

The root mean square of the turbulent velocity fluctuations(u_{rms}) measured by the probe is defined as the square root of the variance of the stream 1 velocity. The integral time scale (τ_{int}) of the velocity fluctuations is determined by extrapolating the power spectral density towards zero frequency. This estimate is equivalent to and has good agreement with the integral of the autocorrelation coefficient curve. By applying Taylor's frozen field hypothesis, the integral length scale (L_{int}) can be calculated as the product of the stream 1 mean velocity and the integral time scale. The turbulent flow field characterization was performed at room temperature ($T = 295$ K) with air and the effects of elevated temperatures and different fluids on $u_{\mathrm{rms}}/\bar{U} = f(Re_{\mathrm{D}})$ and $L_{\mathrm{int}} = f(Re_{\mathrm{D}})$ are accounted for by modifying the mixture viscosity appropriately to determine Re_{D} at the experimental conditions [24]. Finally, the turbulent Reynolds number is defined as the product of the root mean square of the turbulent velocity fluctuations and the integral length scale divided by the kinematic viscosity ($Re_{\mathrm{T}} = u_{\mathrm{rms}} L_{\mathrm{int}}/\nu$).

The turbulent nonpremixed cool flame is tested at a stream 1 flow velocity of $\bar{U} = 2.5$ m/s. At this condition, the velocity fluctuation in stream 1 is measured to be $u_{\mathrm{rms}} = 0.42$ m/s, the integral length scale

is $L_{\text{int}} = 2.98$ mm, the inner diameter Reynolds number is $Re_{\text{D}} = 911$, and the turbulent Reynolds number is $Re_{\text{T}} = 30$. The turbulent Reynolds number is kept low (weak turbulence) to prevent the cool flame from blowing off at the experimental conditions. At elevated pressures, however, the cool flame is expected to stay attached for much higher strain rates and turbulent Reynolds number. The stream 2 flow velocity is $U_2 = 1.0$ m/s, and the stream 3 flow velocity is $U_3 = 0.5$ m/s. All three streams are set to a temperature of $T = 600$ K. Stream 1 contains a mixture of 20% dimethyl ether, 78% nitrogen, and 2% acetone by mole fraction. Stream 2 consists of pure oxygen, and stream 3 consists of air.

2.2. Flame establishment

Turbulent cool flames are formed in the CARAT burner under the conditions given in the previous subsection. A turbulent hot flame is first established and then extinguished after 30-60 seconds using a tetrafluoroethane gas duster. The cool flame forms soon after this quenching process. The existence of the DME cool flame is evident from the strong CH_2O PLIF signal – at the same conditions, a DME unburned mixture does not exhibit any significant CH_2O signal. Thermocouple measurements within the first 15 seconds after the extinction of the hot flame reveal that the flow nearest the wall is temporarily heated by approximately 25 K. The cool flame begins as an attached flame for the first 30-60 seconds, slowly lifts off over the course of a couple of minutes, and then finally rises above the height of the PLIF sheet. All measurements in the sections below are taken when the flame is attached. The use of pure oxygen in the pilot flow extends the range and duration of conditions for which turbulent nonpremixed cool flames can be stabilized but is not strictly necessary, for cool flames were also able to be formed with air in the pilot flow. The cool flames are seen to be highly temperature dependent, forming readily for $T = 600$ K boundary temperatures but not for $T = 550$ K.

2.3. Diagnostic setup and data processing

The turbulent cool flame structure is measured through a combination of CH_2O PLIF [29], acetone PLIF [30], and planar Rayleigh scattering [31]. Figure 2 depicts the diagnostic setup for the CARAT burner. Only two Nd:YAG lasers and two ICCD cameras were available, so a choice had to be made between (a) simultaneous CH_2O PLIF and Rayleigh scattering or (b) simultaneous acetone PLIF and Rayleigh scattering. The CH_2O PLIF and acetone PLIF rely on the same laser (Quantel Q-smart 850) at different harmonics (3rd and 4th, respectively). As outlined in Table 1, the laser used for Rayleigh scattering (Spectra-Physics, lab-170-10) issues a 532 nm beam at an energy of ~ 400 mJ/pulse. After passing through a dichroic mirror, it joins together with the beam from the second laser, as illustrated in Fig. 2. The two beams are then expanded into sheets 30 mm high and 200 μm thick and positioned over the centerline of the burner. A delay generator controls the timing of both lasers and the CH_2O/acetone ICCD camera. Since the CH_2O/acetone

camera can only process images at $\sim$ 2 Hz (due to readout time limitations), the Rayleigh camera's timing is controlled by the CH_2O/acetone camera to ensure that the images are simultaneous.

The Rayleigh scattering images (50-100 per run) were processed into temperature measurements in the following manner. First, a few Rayleigh scattering images were affected by the presence of residual acetone droplets or dust, so a threshold value of approximately 1.25 times the run-averaged maximum signal was used as a cutoff. This ensured that the droplets/dust would be no higher than the threshold value, without altering otherwise locally high values of the Rayleigh scattering signal. The entire run of images was then averaged to obtain a single time-averaged image, and the time-averaged background (minimum value) was subtracted. Next, a correction for the laser power was made in the streamwise direction using a fourth-order polynomial fit to obtain the 2-D images of Rayleigh scattering signal seen in Fig. 3a and Fig. 3b.

This work takes advantage of the fact that, unlike for hot flames, a cool flame's spatial Rayleigh scattering cross section profile is nearly the same as that of an unburned mixture at the same conditions. This is due to the partially oxidizing nature of cool flames and the resulting reactant leakage, and is shown in Fig. 4, where calculated Rayleigh scattering cross sections of a one-dimensional counterflow cool flame and an unburned mixture in physical space (using the values from [32]) are compared. In these flames, the fuel stream contains $X_{N_2} = 0.8$ and $X_{CH_3OCH_3} = 0.2$ and the oxidizer stream contains $X_{O_2} = 1.0$. Both streams have a temperature of 600 K; the pressure is atmospheric, and the strain rate is 400 s^{-1}. These trends hold regardless of the transport model used, for calculations with both detailed transport and unity Lewis numbers were tested. The software and chemical models used for these calculations will be discussed in the following section. Figure 4 also shows the cross section for a hot flame, which is very different from the unburned mixture cross section.

Due to this similarity, it is reasonable to assume that the time-averaged Rayleigh scattering cross sections for an unburned mixture and a cool flame at the same conditions are equal. Using this premise, dividing the time-averaged Rayleigh scattering signal of the unburned mixture by the time-averaged Rayleigh scattering signal of the cool flame gives the two-dimensional time-averaged temperature of the cool flame in Fig. 3c. The only additional assumption this requires is that the unburned mixture has a time-averaged temperature of 600 K. Unfortunately, this method cannot be used to produce instantaneous two-dimensional temperatures, as the instantaneous Rayleigh scattering cross sections of the individual turbulent cool flames cannot be accounted for using the aforementioned method. To measure instantaneous temperature profiles, either the Rayleigh scattering cross section must be held constant throughout the flame [33, 34], or combined Raman-Rayleigh techniques must be used to measure the major species that dominate the Rayleigh scattering signal [26, 32, 35].

The acetone PLIF images are converted into two-dimensional mixture fraction fields by assuming that a linear relationship exists between the acetone mole fraction and the mixture fraction since acetone is mostly

non-reactive in this low-temperature flame. As can be seen in Fig. 5, this assumption is sensible, for a linear fit (with a y-intercept of zero) to the computed acetone mole fraction at $a = 400$ s^{-1} gives an R^2 value of 0.99. Additionally, Fig. 5 also shows that the profile is insensitive to strain rate and thus only needs a single calibration. Like the Rayleigh scattering images, the acetone PLIF images have the background signal subtracted and are corrected for variations in laser power. Additionally, due to the spatial variations in the time-averaged temperature, the time-averaged acetone PLIF signal is corrected for quenching effects at 266 nm and 1 atm [36]. Both the time-averaged uncorrected and corrected mixture fraction fields are shown in Fig. 6. Finally, qualitative two-dimensional images of CH_2O signal are derived from the CH_2O PLIF measurements through the same sequence of background subtraction followed by laser power correction and quenching corrections [37]. Again, both time-averaged uncorrected and corrected PLIF fields are shown in Fig. 7. Since only time-averaged temperatures were obtained through Rayleigh scattering, only time-averaged PLIF signals could be corrected for quenching, leaving RMS measurements uncorrected.

3. Computational configuration and infrastructure

The DNS aims to recreate the experimental configuration as accurately as possible. As a consequence, the computational configuration is also described by Fig. 1, but the burner is only simulated above the $x = 0$ dashed line. Only the statistically stationary jet is studied, and no early time transient behavior or flame ignition will be discussed. Stream 3 is specified as a bulk inflow at the experimental velocity to mimic the effect of the honeycomb mesh. Stream 2 is also specified as a bulk inflow at the experimental velocity but fully develops before exiting the burner. Stream 1 is specified through an auxiliary simulation of unsteady turbulent flow to match the experimental conditions.

The turbulent inflow simulation is of three-dimensional linearly forced [38] isotropic turbulence in a periodic box. The size of the box ($L = 7.31$ mm) is chosen in order to set the integral length scale (L_{int}) to the experimentally measured value. Note that this is required because linear forcing does not allow a length scale of forcing to be chosen independently. The forcing coefficient ($A = 104.7\,\text{s}^{-1}$) is then selected to match the root mean square velocity (u_{rms}) and turbulent Reynolds number (Re_{T}) to the experimental measurements. A two-dimensional plane of data is saved every time-step. Finally, this data is interpolated and used as the inflow for the CARAT simulation with the experimentally measured mean velocity added to the streamwise component. Since the diameter of the nozzle is roughly twice as large as the box size, the velocity field is periodically repeated in the inflow but is visually and statistically absent by the time the flow reaches any measurement or analysis location. The inflow temperatures and species mole fractions are as described in the previous subsection, except that stream 1 does not contain the minor amount of acetone and instead contains $X_{\text{N}_2} = 0.8$ and $X_{\text{CH}_3\text{OCH}_3} = 0.2$.

To simulate the jet, the mass, momentum, species, and temperature evolution equations are solved in

cylindrical coordinates in the low Mach number limit using NGA. A conservative, semi-implicit, iterative algorithm [39] is used, with momentum and pressure Poisson equations updated with a fractional-step scheme [40]. A linearly implicit, approximately factorized scheme [41] is used to solve for species and temperature equations. A second-order central difference scheme is used to discretize all diffusive terms as well as the convective term in the momentum equation. A third-order WENO scheme [42] is used to discretize convective terms in the species and temperature equations. Constant, non-unity Lewis numbers [43, 44] are used, selected as the Lewis numbers computed from a one-dimensional nonpremixed cool flame at the same thermochemical conditions, near the logarithmic center of the cool flame branch of the s-curve. The Lewis numbers change minimally across the entirety of the cool frame branch of the s-curve. The combustion of DME is described with a 56-species detailed chemical mechanism [45] containing low-temperature chemistry. This mechanism was selected for the combination of relatively small size and accuracy at predicting flame limiting phenomena [13].

The cylindrical domain has an axial length of $L_x/D = 12$ with $n_x = 720$ points, a radial length of $L_r/D = 4.6$ with $n_r = 170$ points, and is swept over $\theta = 2\pi$ with $n_\theta = 128$ points. Uniform grid sizing is used throughout the entire axial direction ($\Delta x = 0.25$ mm) as well as in the radial direction ($\Delta r = 0.25$ mm) from the center of the jet until the beginning of the honeycomb mesh region, where it is geometrically stretched at a rate of $S_r = 1.1$. The grid sizing is selected to ensure that the Kolmogorov scale is fully resolved everywhere turbulence can be present in the domain, with $\max\left(\Delta x, \Delta r, r\Delta\theta\right)/\eta \approx 1.4$ [46]. Additionally, the grid sizing follows previous work [47, 48] to ensure that the flame resolution corresponds to approximately 10 points across the thinnest reaction layers, which occur immediately after exiting the nozzle. Adiabatic, non-slip walls are used to model the nozzle. A gravitational body force is applied in the axial direction. Statistics are collected from the flame over 400 integral time scales, equivalent to about 6.5 flow-through time scales.

One-dimensional steady nonpremixed flame solutions are computed with the same chemical mechanism discussed above using FlameMaster [49]. Unity effective Lewis numbers are used in these calculations, with justification provided later.

4. Results

4.1. Global flame structure

The stabilization mechanism for the flame in the experiment is flame anchoring to the wall of the nozzle. However, the simulation as outlined in the previous sections results in a lifted flame stabilized by a partially premixed edge flame about 15 mm above the nozzle exit. This is evident in Fig. 8, where mean formaldehyde profiles from both the DNS and the experiment are shown. The cause of this difference in stabilization mechanism is now explored.

The scalar dissipation rate is largest at the exit of the nozzle and has a value of $\overline{\chi}_{\max} = 91.5\,\mathrm{s}^{-1}$. This value is compared to the s-curve for a one-dimensional flame using streams 1 and 2 as boundary conditions in Fig. 9. This figure shows the cool flame branch of the s-curve, indicating that the mean scalar dissipation rate near the wall is extremely close to the cool flame extinction point. In addition, the scalar dissipation rate is a fluctuating quantity near the nozzle exit and can therefore instantaneously increase even higher, thereby potentially leading to flame extinction. However, the arguments used above should also hold for the experiment since the nozzle exit scalar dissipation rate is controlled by the wall thickness, which is the same in both configurations. Two potential causes are now explored. The influence of the chemical mechanism is first explored, followed by deeper examination of boundary conditions.

4.1.1. Chemical mechanism

While DNS solves the governing equations for a non-reacting flow without approximation (neglecting any discretization errors), it cannot do the same for a reacting flow. Specifically, the chemical mechanism used to describe the chemical source terms in the species and energy equations will always be a model of the underlying combustion chemistry. This is a concern when working with low-temperature chemistry because mechanisms that can account for this chemistry are necessarily larger than those that do not and must, for computational tractability, be reduced in size. This reduction is usually done such that a subset of chosen quantities are still accurate in a specific range of thermochemical conditions, thus limiting the generality of the mechanism and increasing the error for other quantities and away from the operating range. The importance of chemical mechanisms is now briefly explored in the context of whether they can account for the discrepancy between simulation and experiment.

The 56 species chemical mechanism used throughout this work will be referred to as the nominal Wang model [45]. Additionally, a different 56 species chemical mechanism will be referred to as the alternative Zhao model [50]. S-curves using the same thermochemical and boundary conditions as the rest of this work were generated using the two mechanisms, with the cool flame branches of the s-curves shown in Fig. 10. The alternative Zhao mechanism predicts a higher temperature at all scalar dissipation rates but, more importantly, has roughly a factor of three higher extinction scalar dissipation rate. This is significant because this model would then always predict less cool flame extinction than the Wang model. Had the DNS been conducted using the alternative Zhao mechanism, the flame would have likely been attached, consistent with the experiment.

However, anchoring the flame with the alternate mechanism does not imply that the mechanism is more accurate. Recent work [13] has examined both the Wang and Zhao models and compared them to experimental measurements of extinction in laminar DME nonpremixed counterflow flames. While the two mechanisms both did well describing hot flame extinction, the alternative Zhao model was found to be far worse at describing cool flame extinction, and the nominal Wang model was among the best tested. Additionally, the

higher temperatures from the Zhao model are inconsistent with the experimental measurements that will be shown later. For these reasons, the nominal Wang mechanism is deemed to be more appropriate, and the anchoring of the flame that would have been achieved with the alternative Zhao mechanism is deemed to be coincidental.

4.1.2. Boundary conditions

As mentioned earlier, the experimental initialization of the cool flame increases the inlet temperature to extremes of up to 625 K, especially directly above the nozzle wall. This increase in temperature has the potential to extend the extinction limits of the cool flame near the burner. The heated nozzle is accounted for in one-dimensional nonpremixed flame solutions by increasing the temperature boundary conditions to 610 K, which is an estimate of the average temperature increase from thermocouple readings. The effect of this boundary condition change is shown in Fig. 11, where the s-curve for 600 K boundaries is now compared to one with the adjusted 610 K boundary temperatures. While the increase in extinction scalar dissipation rate appears only moderate, a second DNS with stream 1 and 2 inlet temperatures adjusted to 610 K shows a flame anchored to the burner. This is demonstrated in Fig. 12, which shows a comparison between temperature in the original DNS and the modified DNS with adjusted boundary conditions, indicating that the new DNS contains a fully nonpremixed burner-stabilized flame. While this modified boundary condition mimics the heat transfer effects from the wall, it should be noted that the true physical boundary conditions would instead be a thermal boundary layer created by a 600 K flow over heated walls

In hot flames, a boundary temperature error of 10 K would be negligible compared to the 2000 K increase in temperature from reactants to products. However, in a cool flame where the temperature increases no more than about 150 K, this small increase in temperature is almost 7% of the total temperature rise. This percentage would be roughly equivalent to a 150 K temperature rise in a typical hot flame, which would certainly not be negligible. Therefore, while it may seem as though this flame is extremely sensitive to boundary conditions, this is only true in an absolute sense, not in a relative sense.

4.2. Detailed flame structure

Experimental measurements are taken over a narrow window between approximately $x/D = 1.5$ and 2.0, are averaged in the axial direction to reduce noise, and are reported as a function of radial distance only. DNS results are taken from the case with adjusted boundary conditions and are processed over the same window in the same way for comparison. Experimental measurements for both positive and negative radial distance are not averaged but are instead shown separately to emphasize the amount of variation in the experiment.

Mean measurements of temperature, mixture fraction, and formaldehyde from both the experiment and the DNS are reported in Fig. 13(a-c). The qualitative and quantitative trends in each of the three quanti-

ties are well predicted by the DNS. DNS results for temperature and mixture fraction are well within the experimental uncertainty of the experiment. Formaldehyde is difficult to compare quantitatively, given that the experiment measures signal strength rather than the mass fraction obtained from the DNS. However, the large amount of centerline formaldehyde measured by the experiment is due to slower jet spreading and shorter flame height than in the DNS. DNS statistics just half an inlet diameter further downstream show similar centerline formaldehyde mean and RMS values.

Second-order statistics of mixture fraction and formaldehyde are shown in Fig. 13(d-e). The RMS of temperature was not calculated for the experiment because instantaneous temperature was not measured. Again, qualitatively and quantitatively, both experiment and simulation results agree well. However, just as for the mean formaldehyde, the experiments show large values at the centerline for the RMS, while the simulation is near zero. These results further suggest that the DNS is slightly over predicting the flame height compared to the experiment, which is likely due to the specification of the thermal boundary conditions.

5. Turbulent combustion modeling

The good agreement of temperature, mixture fraction, and formaldehyde profiles is justification for the use of the DNS and chemical mechanism to study nonpremixed cool flames from a modeling perspective. The subsequent sections will first examine the validity of using unity effective Lewis numbers for modeling of this flame and then explore the use of manifold-based models for turbulent nonpremixed cool flames.

5.1. Effective Lewis numbers

The validity of unity Lewis numbers in one-dimensional flame solutions for comparison with conditional statistics of non-unity Lewis numbers turbulent hot flames has previously been well established [51]. Specifically, when the Reynolds number is sufficiently large, turbulent diffusion overwhelms molecular diffusion and mixes everything indiscriminately. However, "large" Reynolds number in this context is usually at least an entire order of magnitude higher than in the configuration currently considered. Previous work [51] has used a differential diffusion parameter (z) to assess how accurate an effective unity Lewis number model would be. The differential diffusion parameter can be defined as the absolute value of the difference between the elemental mixture fraction based on hydrogen (Z_H) and carbon (Z_C):

$$z = |Z_H - Z_C|. \tag{1}$$

These two elemental mixture fractions are defined as

$$Z_j = \left(\sum_k a_{jk} \frac{W_j}{W_k} Y_k \right) \left(n_j \frac{W_j}{W_{C_2H_6O}} Y_{C_2H_6O,1} \right)^{-1}, \tag{2}$$

where j represents either the element H or C, a_{jk} is the number of atoms of element j in species k, W represents the molar mass (either elemental or molecular), Y_k represents the mass fraction of species k, n_j

represents the number of atoms of element j per molecule of DME in the inner stream (6 for H, 2 for C), and $Y_{C_2H_6O,1}$ is the mass fraction of DME in the inner fuel stream. The term in the second set of parentheses of this equation simply acts to normalize the mixture fraction between zero and one.

When the differential diffusion parameter is small, a unity effective Lewis number approximation is valid. The parameter is calculated locally everywhere for the DNS and is plotted for a single instantaneous planar snapshot in Fig. 14. The maximum value of the parameter in the entire domain is found to be on the order of $z_{\max} = 10^{-4}$, which is negligibly small. Therefore, the unity effective Lewis number assumption is used for all one-dimensional calculations in this work.

The reasoning for why a relatively "low" Reynolds number cool flame would have effective unity Lewis numbers is as follows. In a hot flame, the Reynolds number needs to be large because the temperature difference across a hot flame increases the viscosity by one order of magnitude, leading to an order of magnitude reduction of Reynolds number in the flame. By their very nature, cool flames exhibit much less of a temperature increase and so do not have such a significantly reduced Reynolds number in the flame. Therefore, a turbulent cool flame with an order of magnitude smaller Reynolds number as measured in the non-reacting region as compared with a hot flame will have a comparable Reynolds number within the flame. This is illustrated in Fig. 15, where the ratio of kinematic viscosity from the inner fuel flow (ν_1) and the kinematic viscosity as a function of mixture fraction, is plotted against mixture fraction for a cool flame and a hot flame at the same thermochemical conditions and scalar dissipation rate. For a constant characteristic velocity and length scale, this ratio describes the attenuation factor of the Reynolds number as a function of mixture fraction. The figure shows that, while the attenuation is small across the entire cool flame, there are large changes across the hot flame, as described earlier. Therefore, the unity effective Lewis number approximation is expected to be valid for turbulent cool flames, even for Reynolds numbers considered small in the context of hot flames.

5.2. Comparison to manifold based models

Temperature and formaldehyde mass fraction from the DNS are compared to one-dimensional nonpremixed flame solutions in Fig. 16. The scalar dissipation rate profile used in the one-dimensional calculations is taken as the conditional mean scalar dissipation rate from the DNS at $x/D = 2$, rather than the often used analytical expression for a nonpremixed counterflow flame. The importance of using this dissipation rate profile in turbulent nonpremixed cool flames is discussed in previous work [23]. One-dimensional solutions at scalar dissipation rates two geometric standard deviations away (taken from the DNS) are also shown in Fig. 16 to help compensate for the non-linearities associated with the fluctuating dissipation rate, which is especially important for formaldehyde. There are minor differences on the lean side, which can be attributed to the use of a two-stream model to describe this three-stream system. A more rigorous three stream analysis could become necessary if the effect of the third-stream was stronger [52, 53].

One noteworthy aspect of these results is that the maximum temperature ($T_{\max}$) is shifted slightly lean relative to stoichiometric mixture fraction ($Z_{\rm st} = 0.62$). An off-stoichiometric $T_{\max}$ is not unheard of [54], especially in cases involving oxyfuel combustion [55] or MILD combustion [56]. However, one unusual trait of cool flames is the significant motion of the flame in mixture fraction space with changing scalar dissipation rate but constant boundary conditions. Figure 17 shows this occurring for computed one-dimensional nonpremixed cool flames with $X_{\rm DME} = 0.2$ and $X_{\rm N_2} = 0.8$ on the fuel side and $X_{\rm O_2} = 1.0$ on the oxidizer side. In these calculations, $T_{\max}$ is located close to $Z_{\rm st}$ for low dissipation rates, but on the considerably lean side of $Z_{\rm st}$ for high scalar dissipation rates. The location of peak formaldehyde is considerably rich for low scalar dissipation rates and lean for high dissipation rates, crossing through $Z_{\rm st}$ at intermediate dissipation rates. Previous simulations of droplet combustion have found similar behavior, showing that nonpremixed cool flames are much more likely to reside further from $Z_{\rm st}$ than nonpremixed hot flames [57].

This motion in mixture fraction space is due to the partially oxidizing nature of cool flames. Only two O_2 additions to DME are required for low-temperature chain branching; consequently, at low dissipation rates (i.e., high residence times), DME has sufficient time to react with two O_2 molecules before reaching Z_{st}. However, for high dissipation rates, most of the DME does not have time to react until it is already on the lean side of $Z_{\rm st}$. Therefore, the motion in mixture fraction space of cool flames is caused by the significant fuel and oxidizer leakage across $Z_{\rm st}$. An alternative way of thinking about this is in terms of the activation energy. Nonpremixed hot flames have large activation energies and are therefore much more temperature-dependent than residence time-dependent, but nonpremixed cool flames with lower activation energies experience competition between the two. Therefore, the location of nonpremixed hot flames tends to be very close to $Z_{\rm st}$, but the location of nonpremixed cool flames can be a strong function of the strain rate (residence time).

Figure 17 also shows the mixture fraction where conditional means of temperature and formaldehyde are at a maximum in the DNS. This data is taken at different locations downstream, with the conditional mean stoichiometric scalar dissipation rate decreasing away from the nozzle. The figure shows good agreement between the one-dimensional solutions and the DNS data, including the crossover from lean to rich that occurs for formaldehyde. The slight disagreement is due to the difference in scalar dissipation rate profiles between the one-dimensional solutions, which use an analytical closure for the profile, and the DNS, where the profile is calculated from the mixture fraction field. Motion in mixture fraction space of turbulent nonpremixed cool flames has previously been observed in DNS [19]. However, whereas the mechanism for such behavior was previously identified as a "deflagration", this analysis shows that the motion occurs due to a purely nonpremixed flame mechanism, namely the decay of scalar dissipation rate. The ability of one-dimensional nonpremixed flame solutions to predict this motion in mixture fraction space is an important demonstration that manifold-based models can describe turbulent nonpremixed cool flames.

6. Conclusions

A well-defined CARAT burner has been developed for the investigation of turbulent nonpremixed DME cool flames for direct comparison to computational studies. Turbulent nonpremixed cool flames have been tested by employing CH_2O PLIF, acetone PLIF, and planar Rayleigh scattering. Two-dimensional mixture fraction and temperature measurements have been derived from the acetone PLIF and Rayleigh scattering signals, respectively. The similarities between cool flames and unburned mixtures allow for quantitative temperature measurements without the need for constant Rayleigh scattering cross sections

A DNS database of an isolated turbulent nonpremixed cool flame based on the experimental CARAT burner has been created. The global flame structure was found to be dependent on the inlet boundary conditions, such that a 10 K difference in inflow temperature switched the flame from being lifted to anchored at the burner. Comparisons of the DNS to experimental measurements found good agreement for temperature and mixture fraction profiles in physical space with the adjusted boundary condition.

Examination of a differential diffusion parameter in the DNS found that an effective Lewis number of unity was valid for this configuration, even though the Reynolds number is considerably lower than typical values that support unity effective Lewis numbers in hot flames. This is attributed to the very low change in temperature, viscosity, and therefore Reynolds number across a cool flame compared to a hot flame. One-dimensional nonpremixed flame solutions were shown to very closely match conditional means from the DNS. Motion of the flame in mixture fraction space was examined and also found to be well described by one-dimensional flame solutions, indicating that the motion is due to a purely nonpremixed flame mechanism.

This follows up on previous work [23], where manifold-based models were shown to model turbulent nonpremixed cool flames well. However, this work makes an even stronger argument by actually comparing conditional statistics rather than examining only local instantaneous states. The excellent agreement between profiles provides evidence that, fundamentally, there is no special difference between the physics of turbulent combustion in cool and hot flames, and the same reduced-order manifold modeling approaches can be utilized for both.

7. Acknowledgements

AGN and MEM gratefully acknowledge financial support from the Army Research Office (ARO) grant W911NF-17-1-0391 and valuable support in the form of computational time on the TIGRESS high performance computer center at Princeton University, which is jointly supported by the Princeton Institute for Computational Science and Engineering (PICSciE) and the Princeton University Office of Information Technology's Research Computing Department. CBR, ORY, and YJ would like to acknowledge funding from the NETL UTSR program under DOE award DEFE0011822, NSF grant CBET-1507358, and ARO grant

W911NF-16-1-0076. KK, MKF, and MH acknowledge support from AFOSR grant FA9550-16-1-0170. The authors also thank Dr. Christopher Abram for insightful discussions.

References

[1] S. A. Skeen, J. Manin, L. M. Pickett, Simultaneous formaldehyde PLIF and high-speed schlieren imaging for ignition visualization in high-pressure spray flames, Proc. Combust. Inst. 35 (3) (2015) 3167 – 3174.

[2] R. N. Dahms, G. A. Paczko, S. A. Skeen, L. M. Pickett, Understanding the ignition mechanism of high-pressure spray flames, Proc. Combust. Inst. 36 (2) (2017) 2615 – 2623.

[3] A. Burkert, W. Paa, Ignition delay times of single kerosene droplets based on formaldehyde LIF detection, Fuel 167 (2016) 271 – 279.

[4] A. Fish, I. A. Read, W. S. Affleck, W. W. Haskell, The controlling role of cool flames in two-stage ignition, Combust. Flame 13 (1) (1969) 39 – 49.

[5] J. Pan, H. Wei, G. Shu, Z. Chen, P. Zhao, The role of low temperature chemistry in combustion mode development under elevated pressures, Combust. Flame 174 (2016) 179 – 193.

[6] H. Yamada, K. Suzaki, A. Tezaki, Y. Goto, Transition from cool flame to thermal flame in compression ignition process, Combust. Flame 154 (1) (2008) 248 – 258.

[7] C. B. Reuter, S. H. Won, Y. Ju, Experimental study of the dynamics and structure of self-sustaining premixed cool flames using a counterflow burner, Combust. Flame 166 (2016) 125 – 132.

[8] P. Zhao, W. Liang, S. Deng, C. K. Law, Initiation and propagation of laminar premixed cool flames, Fuel 166 (2016) 477–487.

[9] M. Hajilou, T. Ombrello, S. H. Won, E. Belmont, Experimental and numerical characterization of freely propagating ozone-activated dimethyl ether cool flames, Combust. Flame 176 (2017) 326 – 333.

[10] C. B. Reuter, V. R. Katta, O. R. Yehia, Y. Ju, Transient interactions between a premixed double flame and a vortex, Proc. Combust. Inst. 37 (2) (2019) 1851 – 1859.

[11] Y. Ju, C. B. Reuter, S. H. Won, Numerical simulations of premixed cool flames of dimethyl ether/oxygen mixtures, Combust. Flame 162 (10) (2015) 3580 – 3588.

[12] S. Deng, D. Han, C. K. Law, Ignition and extinction of strained nonpremixed cool flames at elevated pressures, Combust. Flame 176 (2017) 143 – 150.

[13] C. B. Reuter, R. Zhang, O. R. Yehia, Y. Rezgui, Y. Ju, Counterflow flame experiments and chemical kinetic modeling of dimethyl ether/methane mixtures, Combust. Flame 196 (2018) 1 – 10.

[14] V. Nayagam, D. L. Dietrich, P. V. Ferkul, M. C. Hicks, F. A. Williams, Can cool flames support quasi-steady alkane droplet burning?, Combust. Flame 159 (2012) 3583–3588.

[15] O. R. Yehia, C. B. Reuter, Y. Ju, Low-temperature multistage warm diffusion flames, Combust. Flame 195 (2018) 63 – 74.

[16] T. I. Farouk, F. L. Dryer, Isolated n-heptane droplet combustion in microgravity: cool flames - two-stage combustion, Combust. Flame 161 (2) (2014) 565 – 581.

[17] I. Gökalp, G. M. L. Dumas, R. I. Ben-Aïm, Temperature field measurements in a premixed turbulent cool flame, Symp. (Int.) Combust. 18 (1981) 969–976.

[18] D. I. Kolaitis, M. A. Founti, A tabulated chemistry approach for numerical modeling of diesel spray evaporation in a stabilized cool flame environment, Combust. Flame 145 (1) (2006) 259 – 271.

[19] A. Krisman, E. R. Hawkes, M. Talei, A. Bhagatwala, J. H. Chen, A direct numerical simulation of cool-flame affected autoignition in diesel engine-relevant conditions, Proc. Combust. Inst. 36 (2017) 3567 – 3575.

[20] A. Krisman, E. R. Hawkes, J. H. Chen, A parametric study of ignition dynamics at ECN spray a thermochemical conditions using 2D DNS, Proc. Combust. Inst. 37 (4) (2019) 4787 – 4795.

[21] G. Borghesi, A. Krisman, T. Lu, J. H. Chen, Direct numerical simulation of a temporally evolving air/n-dodecane jet at low-temperature diesel-relevant conditions, Combust. Flame 195 (2018) 183 – 202.

[22] B. Savard, H. Wang, A. Teodorczyk, E. R. Hawkes, Low-temperature chemistry in n-heptane/air premixed turbulent flames, Combust. Flame 196 (2018) 71 – 84.

[23] A. G. Novoselov, C. K. Law, M. E. Mueller, Direct Numerical Simulation of turbulent nonpremixed cool flames: Applicability of flamelet models, Proc. Combust. Inst. 37 (2) (2019) 2143 – 2150.

[24] S. H. Won, B. Windom, B. Jiang, Y. Ju, The role of low temperature fuel chemistry on turbulent flame propagation, Combust. Flame 161 (2014) 475–483.

[25] B. Windom, S. H. Won, C. B. Reuter, B. Jiang, Y. Ju, S. Hammack, T. Ombrello, C. Carter, Study of ignition chemistry on turbulent premixed flames of n-heptane/air by using a reactor assisted turbulent slot burner, Combust. Flame 169 (2016) 19 – 29.

[26] R. Cabra, T. Myhrvold, J. Y. Chen, R. W. Dibble, A. N. Karpetis, R. S. Barlow, Simultaneous laser raman-rayleigh-lif measurements and numerical modeling results of a lifted turbulent H2/N2 jet flame in a vitiated coflow, Proc. Combust. Inst. 29 (2) (2002) 1881 – 1888.

[27] S. C. C. Bailey, G. J. Kunkel, M. Hultmark, M. Vallikivi, J. P. Hill, K. A. Meyer, C. Tsay, C. B. Arnold, A. J. Smits, Turbulence measurements using a nanoscale thermal anemometry probe, J. Fluid Mech. 663 (2010) 160179.

[28] M. Vallikivi, A. J. Smits, Fabrication and characterization of a novel nanoscale thermal anemometry probe, J. Microelectromech. Sys. 23 (4) (2014) 899–907.

[29] B. Bäuerle, F. Hoffmann, F. Behrendt, J. Warnatz, Detection of hot spots in the end gas of an internal combustion engine using two-dimensional lif of formaldehyde, Symp. (Int.) Combust. 25 (1) (1994) 135 – 141.

[30] A. Lozano, B. Yip, R. K. Hanson, Acetone: a tracer for concentration measurements in gaseous flows by planar laser-induced fluorescence, Exp. Fluids 13 (6) (1992) 369–376.

[31] D. C. Fourguette, R. M. Zurni, M. B. Long, Two-dimensional Rayleigh thermometry in a turbulent nonpremixed methane-hydrogen flame, Combust. Sci. Technol. 44 (5-6) (1986) 307–317.

[32] F. Fuest, R. S. Barlow, J.-Y. Chen, A. Dreizler, Raman/Rayleigh scattering and CO-LIF measurements in laminar and turbulent jet flames of dimethyl ether, Combust. Flame 159 (8) (2012) 2533 – 2562.

[33] V. Bergmann, W. Meier, D. Wolff, W. Stricker, Application of spontaneous Raman and Rayleigh scattering and 2D LIF for the characterization of a turbulent CH4/H2/N2 jet diffusion flame, Appl. Phys. B 66 (4) (1998) 489–502.

[34] A. Soika, F. Dinkelacker, A. Leipertz, Measurement of the resolved flame structure of turbulent premixed flames with constant reynolds number and varied stoichiometry, Symp. (Int.) Combust. 27 (1) (1998) 785 – 792.

[35] A. R. Masri, R. W. Dibble, R. S. Barlow, The structure of turbulent nonpremixed flames revealed by Raman-Rayleigh-LIF measurements, Prog. Energy Combust. Sci. 22 (4) (1996) 307 – 362.

[36] M. C. Thurber, F. Grisch, B. J. Kirby, M. Votsmeier, R. K. Hanson, Measurements and modeling of acetone laser-induced fluorescence with implications for temperature-imaging diagnostics, Appl. Opt. 37 (21) (1998) 4963–4978.

[37] T. Metz, X. Bai, F. Ossler, M. Aldén, Fluorescence lifetimes of formaldehyde (H2CO) in the $\tilde{A}^1A_2 \rightarrow \tilde{X}^1A_1$ band system at elevated temperatures and pressures, Spectrochim. Acta A 60 (5) (2004) 1043 – 1053.

[38] C. Rosales, C. Meneveau, Linear forcing in numerical simulations of isotropic turbulence: Physical space implementations and convergence properties, Phys. Fluids 17 (2005) 095106.

[39] O. Desjardins, G. Blanquart, G. Balarac, H. Pitsch, High order conservative finite difference scheme for variable density low mach number turbulent flows, J. Comput. Phys. 227 (2008) 7125–7159.

[40] J. Kim, P. Moin, Application of a fractional-step method to incompressible Navier-Stokes equations, J. Comput. Phys. 59 (2) (1985) 308 – 323.

[41] J. F. MacArt, M. E. Mueller, Semi-implicit iterative methods for low mach number turbulent reacting flows: Operator splitting versus approximate factorization, J. Comput. Phys. 326 (2016) 569–595.

[42] G.-S. Jiang, C.-W. Shu, Efficient implementation of weighted ENO schemes, J. Comput. Phys. 126 (1) (1996) 202 – 228.

[43] H. Pitsch, N. Peters, A consistent flamelet formulation for non-premixed combustion considering differential diffusion effects, Combust. Flame 114 (1998) 26–40.

[44] N. Burali, S. Lapointe, B. Bobbitt, G. Blanquart, Y. Xuan, Assessment of the constant non-unity Lewis number assumption in chemically-reacting flows, Combust. Theory Model. 20 (2016) 632–657.

[45] Z. Wang, X. Zhang, L. Xing, L. Zhang, H. F., K. Moshammer, F. Qi, K. Kohse-Höinghaus, Experimental and kinetic modeling study of the low- and intermediate-temperature oxidation of dimethyl ether, Combust. Flame 162 (4) (2015) 1113 – 1125.

[46] P. K. Yeung, S. B. Pope, Lagrangian statistics from direct numerical simulations of isotropic turbulence, J. Fluid Mech. 207 (1989) 531586.

[47] J. F. MacArt, T. Grenga, M. E. Mueller, Effects of combustion heat release on velocity and scalar statistics in turbulent premixed jet flames at low and high Karlovitz numbers, Combust. Flame 191 (2018) 468 – 485.

[48] E. R. Hawkes, O. Chatakonda, H. Kolla, A. R. Kerstein, J. H. Chen, A petascale direct numerical simulation study of the modelling of flame wrinkling for large-eddy simulations in intense turbulence, Combust. Flame 159 (8) (2012) 2690 – 2703.

[49] H. Pitsch, FlameMaster, a C++ computer program for 0D combustion and 1D laminar flame calculations (1998).

[50] Z. Zhao, M. Chaos, A. Kazakov, F. L. Dryer, Thermal decomposition reaction and a comprehensive kinetic model of dimethyl ether, Int. J. of Chem. Kinet. 40 (1) (2008) 1–18.

[51] R. S. Barlow, J. H. Frank, A. N. Karpetis, J.-Y. Chen, Piloted methane/air jet flames: Transport effects and aspects of scalar structure, Combust. Flame 143 (2005) 433–449.

[52] M. Ihme, Y. C. See, LES flamelet modeling of a three-stream MILD combustor: Analysis of flame sensitivity to scalar inflow conditions, Proc. Combust. Inst. 33 (1) (2011) 1309 – 1317.

[53] B. A. Perry, M. E. Mueller, A. R. Masri, A two mixture fraction flamelet model for large eddy simulation of turbulent flames with inhomogeneous inlets, Proc. Combust. Inst. 36 (2) (2017) 1767 – 1775.

[54] C. K. Law, A. Makino, T. F. Lu, On the off-stoichiometric peaking of adiabatic flame temperature, Combust. Flame 145 (4) (2006) 808 – 819.

[55] A. Sevault, M. Dunn, R. S. Barlow, M. Ditaranto, On the structure of the near field of oxy-fuel jet flames using Raman/Rayleigh laser diagnostics, Combust. Flame 159 (11) (2012) 3342 – 3352.

[56] J. A. M. Sidey, E. Mastorakos, Simulations of laminar non-premixed flames of methane with hot combustion products as oxidiser, Combust. Flame 163 (2016) 1 – 11.

[57] G. Paczko, N. Peters, K. Seshadri, F. A. Williams, The role of cool-flame chemistry in quasi-steady combustion and extinction of n-heptane droplets, Combust. Theory Model. 18 (2014) 515–531.

[58] A. E. Lutz, R. J. Kee, J. F. Grcar, F. M. Rupley, OPPDIF: A fortran program for computing opposed-flow diffusion flames (1997).

[59] U. Burke, K. P. Somers, P. O'Toole, C. M. Zinner, N. Marquet, G. Bourque, E. L. Petersen, W. K. Metcalfe, Z. Serinyel, H. J. Curran, An ignition delay and kinetic modeling study of methane, dimethyl ether, and their mixtures at high pressures, Combust. Flame 162 (2) (2015) 315 – 330.

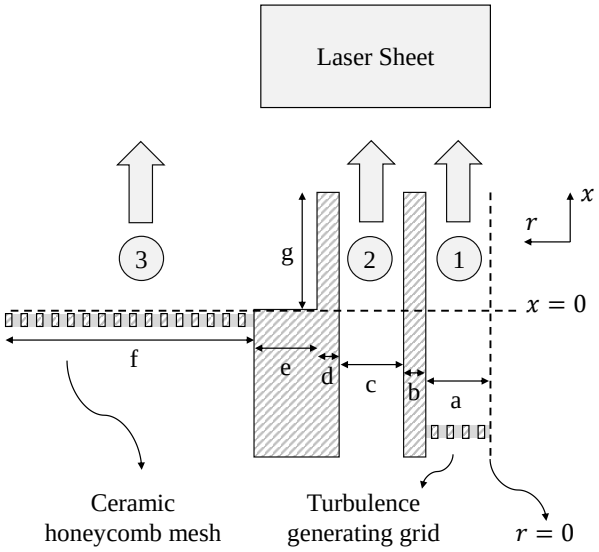

a (mm)	b (mm)	c (mm)	d (mm)	e (mm)	f (mm)	g (mm)
7.5	1.0	2.0	2.0	4.5	38.0	8.0

Figure 1: Experimental configuration for the CARAT burner. The simulation domain is the area above the $x = 0$ dashed line.

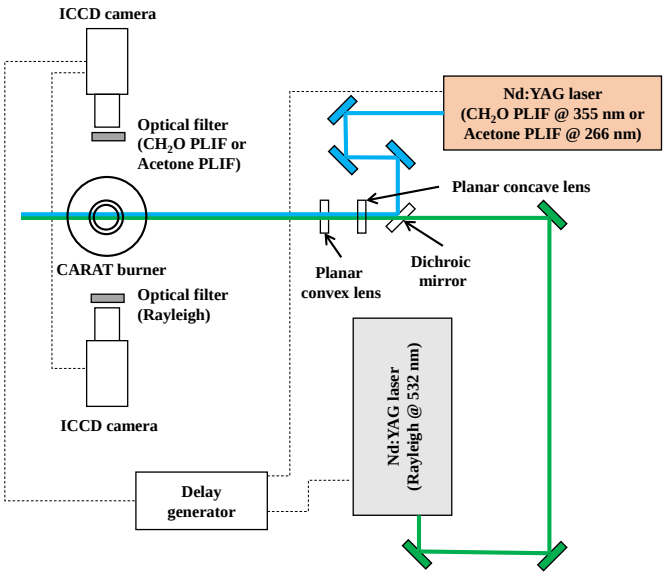

Figure 2: Diagnostic setup for the CARAT burner, employing two lasers and two cameras.

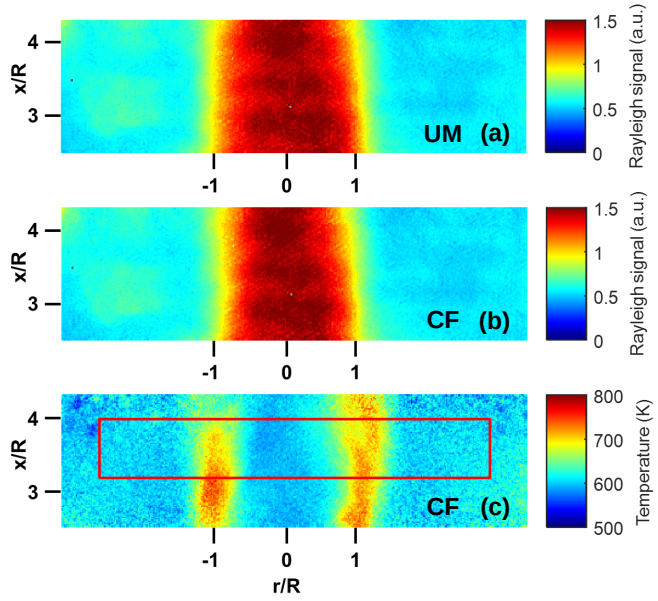

Figure 3: Time-averaged (a) Rayleigh scattering signal for an unburned mixture, (b) Rayleigh scattering signal for a cool flame, and (c) temperature for a cool flame. The red box indicates where the time-averaged statistics will be computed.

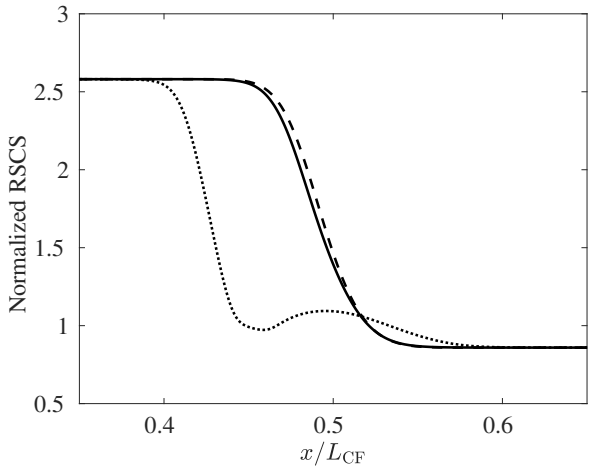

Figure 4: Computed Rayleigh scattering cross section (RSCS) profiles for hot flames (dotted), cool flames (solid), and unburned mixtures (dashed) in the one-dimensional nonpremixed counterflow configuration in physical space normalized by counterflow separation distance. The RSCS values are normalized to the value for nitrogen.

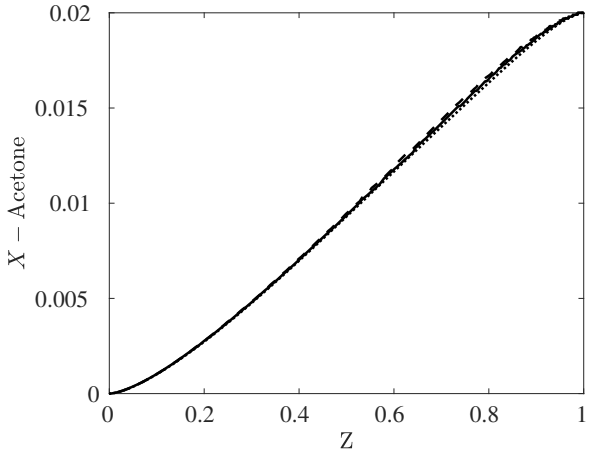

Figure 5: Computed acetone profiles for cool flames at $a = 100$ s^{-1} (dotted), $a = 200$ s^{-1} (solid), and $a = 400$ s^{-1} (dashed) in a laminar nonpremixed counterflow configuration. Acetone chemistry is captured by using the OPPDIF module [58] of the CHEMKIN package with the Burke model [59], only for this calculation.

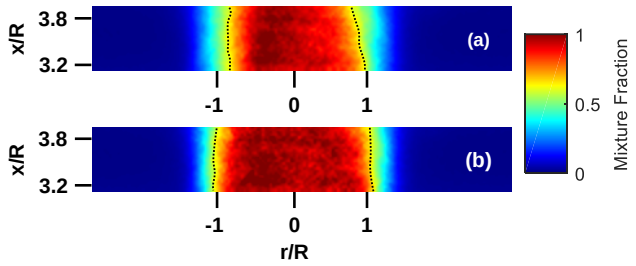

Figure 6: Time-averaged (a) uncorrected and (b) quenching-corrected mixture fraction. The dotted lines indicate the time-averaged stoichiometric mixture fraction contour.

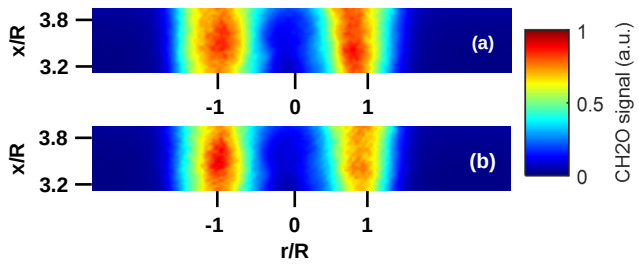

Figure 7: Time-averaged (a) uncorrected and (b) quenching-corrected CH_2O PLIF signal.

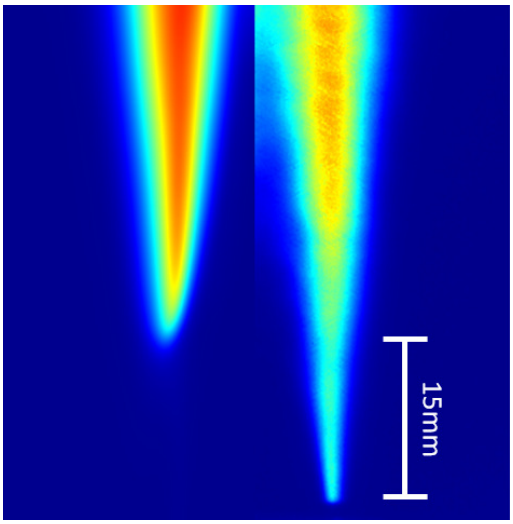

Figure 8: DNS (left) and experimental PLIF (right) profiles of mean formaldehyde slightly above the nozzle.

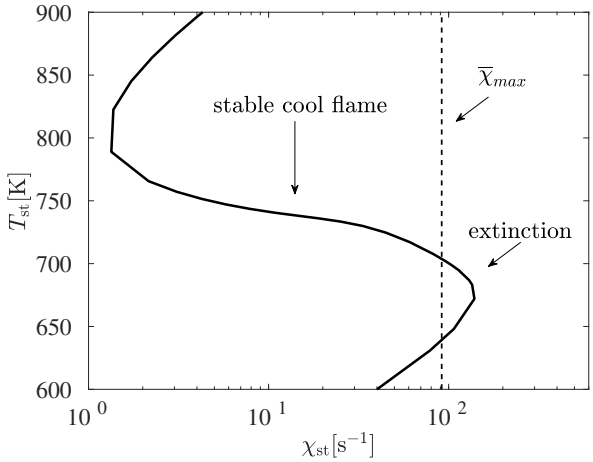

Figure 9: Solid line shows the cool flame branch of the s-curve, and the dashed line shows the value of $\overline{\chi}_{\max}$ at Z_{st} from the DNS. Extinction is on the right, and ignition is on the left.

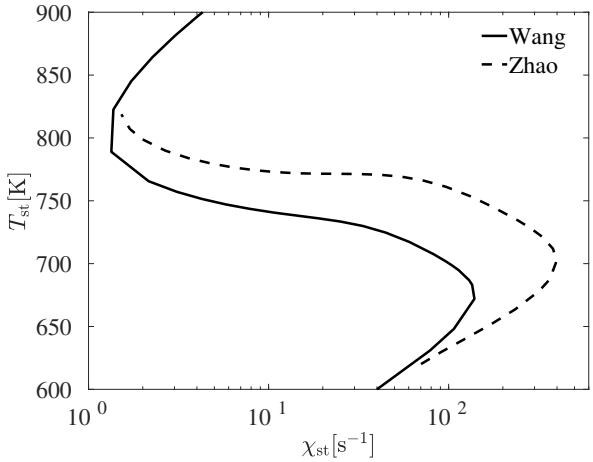

Figure 10: Comparison of the cool flame branch of the s-curve generated using Wang mechanism (solid) and Zhao mechanism (dashed).

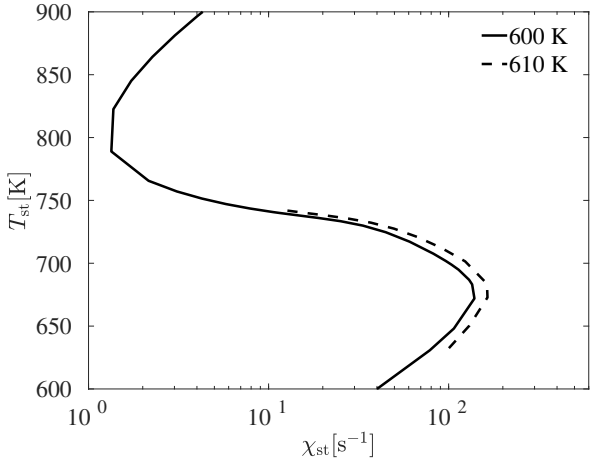

Figure 11: Comparison of cool flame branch of s-curve for thermal boundaries at 600 K (solid) and 610 K (dashed).

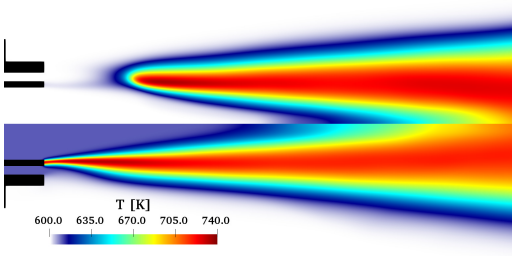

Figure 12: Mean temperature field for a subset of the domain where the stream 1 and 2 inlet temperatures are 600 K (top half) and 610 K (bottom half).

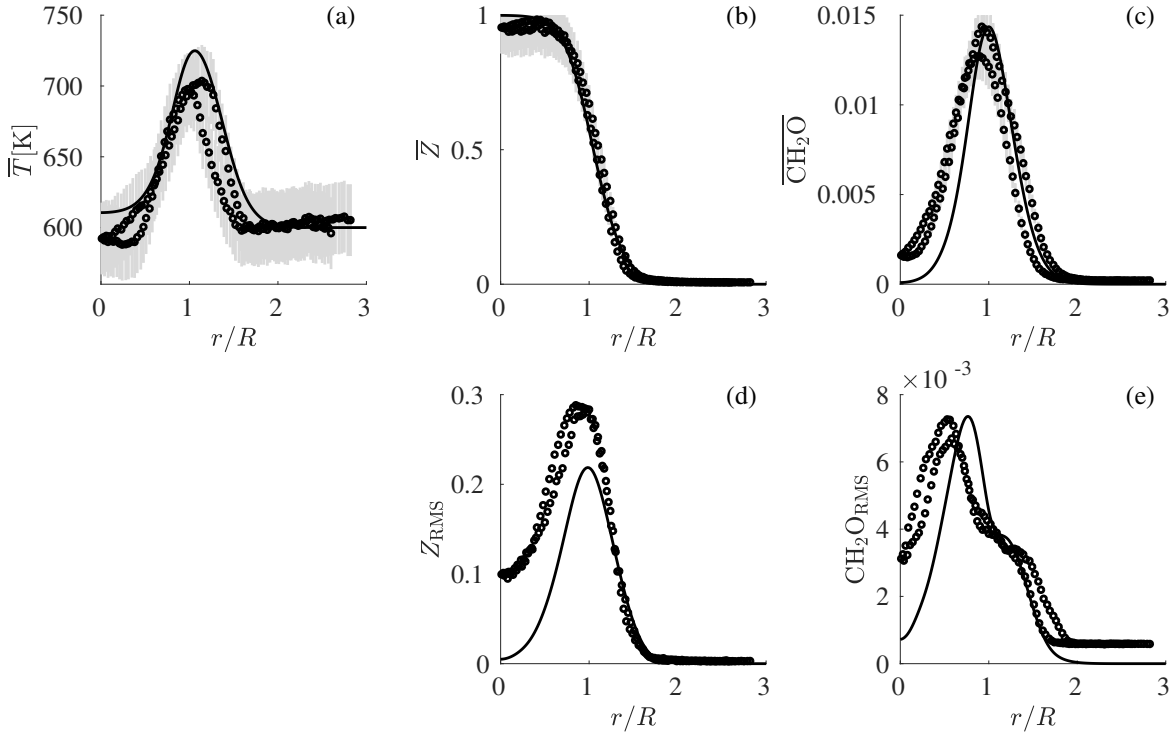

Figure 13: DNS statistics (solid line) and experimental measurements (circles) in physical space, showing mean temperature (a), mixture fraction (b), and formaldehyde (c) and RMS mixture fraction (d) and formaldehyde (e). First-order statistics are reported with experimental errors (±25 K, ±10 %, ±10 % respectively) shown in light grey. For formaldehyde, note that the DNS shows mass fraction, while the experiment shows signal intensity normalized to match the DNS maximum. Experimental measurements for both positive and negative radial distance are shown separately to emphasize variation in the experiment.

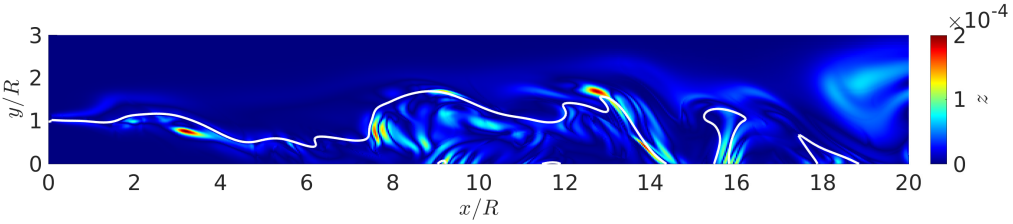

Figure 14: Instantaneous snapshot of differential diffusion parameter ($z = |Z_H - Z_C|$) in physical space, along with the stoichiometric mixture fraction iso-contour (solid white).

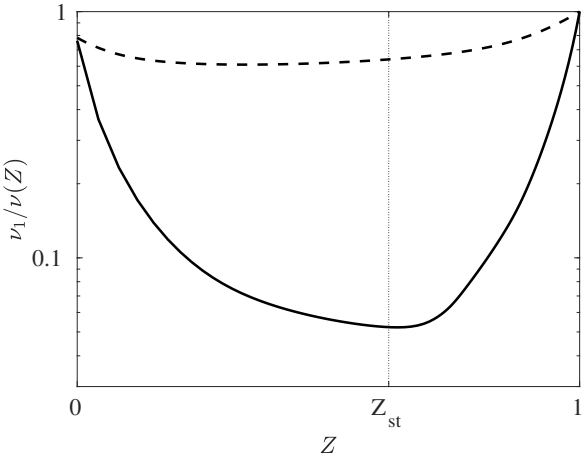

Figure 15: Normalized kinematic viscosity ratio across a cool flame (dashed) and a hot flame (solid) from one-dimensional flame solutions both at the thermochemical conditions used throughout this work and scalar dissipation rate at $x/D = 2$ from the DNS.

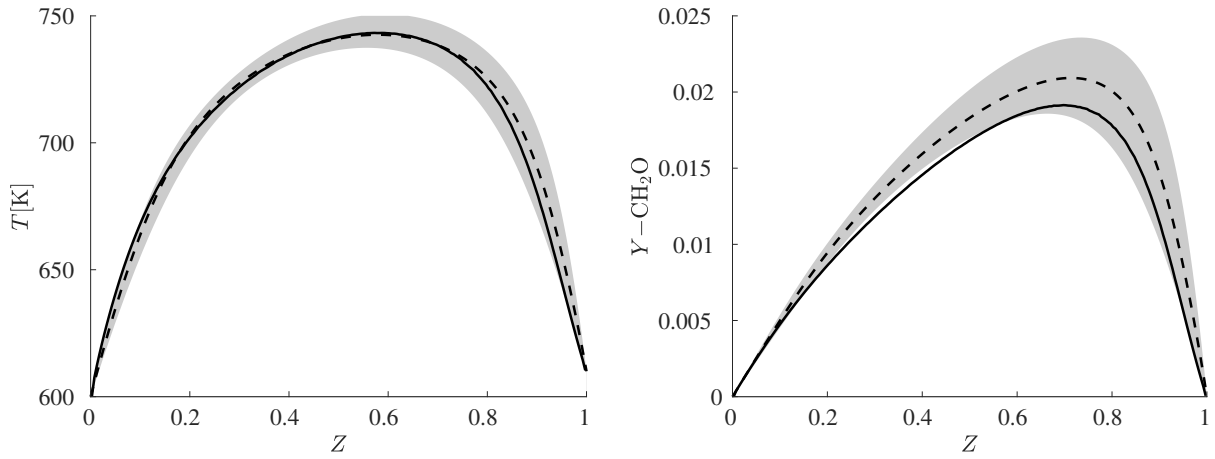

(a) Temperature

(b) Formaldehyde mass fraction

Figure 16: Conditional mean temperature and formaldehyde mass fraction from the DNS (solid) compared to one-dimensional nonpremixed flame solutions (dashed) at $x/D = 2$. The range of one-dimensional solutions corresponding to two geometric standard deviations of scalar dissipation rate from the DNS is shown in grey.

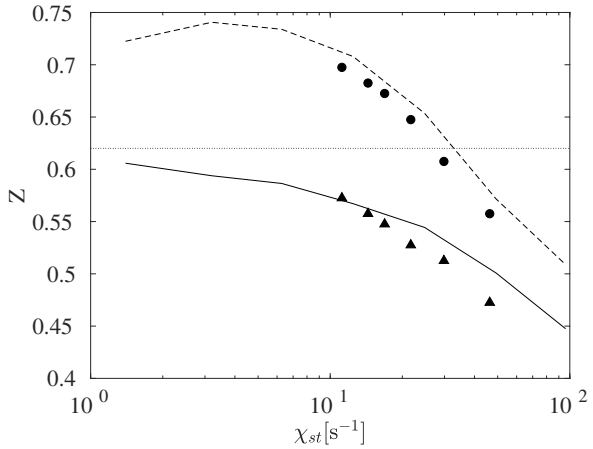

Figure 17: Mixture fraction at maximum temperature (solid line) and formaldehyde (dashed line) from one-dimensional non-premixed flame solutions over a range of stoichiometric scalar dissipation rates. Locations of conditional mean maxima of temperature (triangles) and formaldehyde (circles) from the DNS are also shown at multiple downstream locations. The horizontal dotted line denotes $Z_{\mathrm{st}} = 0.62$.

Technique	**Wavelength**	**Laser**	**Energy/pulse**	**Filter**	**Camera**
Rayleigh scattering	532 nm	Spectra-Physics lab-170-10	400 mJ	BP532-10	Princeton Instruments PI-Max
Acetone PLIF	266 nm	Quantel Q-smart 850	160 mJ	WG-305	
CH_2O PLIF	355 nm		200 mJ	GG-395	

Table 1: List of diagnostic techniques, laser properties, filters, and cameras for this study.